Available online at www.sciencedirect.com
SCIENCE DIRECT®
ELSEVIER
International Journal of Solids and Structures 42 (2005) 3655–3676
INTERNATIONAL JOURNAL OF SOLIDS and STRUCTURES
www.elsevier.com/locate/ijsolstr

Ductile tearing and discrete void effects on cleavage fracture under small-scale yielding conditions

Jason P. Petti, Robert H. Dodds Jr. *

Department of Civil and Environmental Engineering, University of Illinois, Urbana, IL 61801, USA

Received 2 November 2004

Abstract

Over the mid-to-upper region of the ductile-to-brittle transition region, transgranular cleavage and ductile tearing define two competing failure mechanisms in ferritic steel. At metallurgical scales ($\lesssim 50$ μm), formation and growth of the voids driving ductile crack extension likely alter the local stress fields acting on the smaller inclusions that trigger cleavage fracture. Here we study the effects of void growth on cleavage fracture by modeling discrete cylindrical voids lying on the crack plane ahead of the crack tip within a small-scale yielding (SSY) boundary layer model. These discrete voids have a spacing, D, within a highly refined crack-front region. This enables identification of both single void growth and multiple void growth mechanisms that depend primarily on the initial void porosity, f_0. The crack grows in this model by release of nodal reactions (enforcing zero displacement) along the ligament (symmetry plane) between the blunted crack tip and closest void when the void obtains a specified critical porosity. This process grows the crack in discrete increments of size equal to the length of an intervoid ligament. Continued external loading leads to subsequent void growth and crack extensions through additional node releases. The external loads at the point of each crack extension define the crack growth resistance (J_R) curves. This enables comparison with conventional J_R–Δa curves obtained using computational cell (Gurson–Tvergaard) analyses. The Weibull stress model is then employed to quantify the stress concentration effects on the probability of cleavage fracture. We describe a non-dimensional function, $h(\widehat{J})$, to represent stress concentration effects on the Weibull stress in a convenient framework ($\widehat{J} = J/D\sigma_0$ denotes a non-dimensional loading for SSY analyses). These h-functions also reflect the increase in volume of material sampled as the crack grows from the original tip to the first void, the second void, etc. The h-functions vary with material flow properties, initial porosity (f_0), critical porosity (f_c), Weibull modulus (m), and T-stress (T_σ) or constraint level.
© 2004 Elsevier Ltd. All rights reserved.

Keywords: Ferritic steels; Cleavage fracture; Ductile tearing; Local approach; Weibull stress; Crack growth resistance; Void growth; Finite element modeling

* Corresponding author. Tel.: +1 217 333 3276; fax: +1 217 333 9464.
E-mail address: rdodds@uiuc.edu (R.H. Dodds).

0020-7683/$ - see front matter © 2004 Elsevier Ltd. All rights reserved.
doi:10.1016/j.ijsolstr.2004.11.015

1. Introduction

A competition between transgranular cleavage and ductile tearing mechanisms characterizes the fracture behavior of ferritic steels over the temperature driven ductile-to-brittle transition (DBT) region. At low temperatures in the DBT region, the cleavage mechanism causes particular concern as catastrophic, structural failure generally occurs without significant plastic deformation. Cleavage fracture exhibits a "weakest link" phenomenon wherein one (or more) initiation sites at metallurgical scale inclusions trigger unstable crack extension at the macroscopic scale (Curry and Knott, 1976; Landes and Shaffer, 1980; Wallin et al., 1984; Lin et al., 1986; Mudry, 1987; Beremin, 1983; Lin et al., 1986). This mechanism invokes a strong sensitivity to the volume of material along the (macroscopic) crack front subjected to high stresses and to differences in stress fields that arise from constraint variations (large-scale yielding). As the temperature increases through the transition region, small amounts of ductile tearing often occur prior to the onset of cleavage fracture. Ductile tearing pushes the crack front forward which increases the volume of material sampled at high stress levels and thereby influences the eventual likelihood of failure by cleavage fracture. The ductile tearing process occurs from the coalescence of growing voids ahead of the crack front. At metallurgical scales ($\lesssim 50$ μm), the formation and growth of such voids likely alters the local stress fields acting on the nearby inclusions that trigger cleavage fracture. Exploratory work by Isacsson et al. (1998) and Faleskog and Shih (1997) examines these effects on local stress using unit cell-type models.

Predictions of cleavage fracture in test specimens and structural components can be performed successfully using modified Weibull stress, or Beremin (Mudry, 1987; Beremin, 1983), micromechanical models. These models assume a form for the statistical distribution of microcracks present in small, statistically independent volumes of material located ahead of the crack front with a simple Griffith-type toughness relationship taken for the microcracks. Each small volume experiences loading from the macroscopic (continuum) stress field described, for example, by a local value of maximum (tensile) principal stress. A weighted average of the cumulative failure probability taken over all volumes ahead of a crack front leads to a relatively simple expression for macroscopic failure probability involving a scalar measure of the crack front loading, the so-called Weibull stress, σ_w. The Weibull stress model includes several parameters: a Weibull modulus, m, that characterizes the size distribution of microcracks, a Weibull scale parameter, σ_u, that represents the aggregate microcrack toughness, and often a third parameter to enforce prediction of a threshold toughness at the micro- and/or macroscale.

Xia and Shih (1996) were among the first to incorporate the effects of prior ductile tearing into the Weibull stress approach. They employ a computational cell framework to grow a crack under Mode I conditions with a Gurson–Tvergaard (Gurson, 1977; Tvergaard, 1990) constitutive model to simulate cell softening from void growth. Evaluation of the Weibull stress during crack growth analyses leads to estimates for the probability of cleavage fracture. Others including Ruggieri and Dodds (1996a,b), Gao et al. (1999), Xia and Cheng (1997), Neto and Ruggieri (2001) and Kroon (2001) expanded these efforts to couple the Weibull stress concept (and similar models) with computational cell-type models for ductile growth. These studies model the material (computational cells) at the crack front as a continuum and neglect any potential effects of discrete voids ahead of the crack front. Numerical models (Isacsson et al., 1998; Faleskog and Shih, 1997) of discrete voids suggest that the stress concentrations around these voids will influence the crack-front stress fields, the associated Weibull stress and there cumulative failure probability distributions.

Rice and Johnson (1970), McMeeking (1977), Aravas and McMeeking (1985), and Tvergaard and Hutchinson (1992, 2002) among others, have investigated the growth of discrete void(s) located ahead of a blunting crack tip. Here we study discrete void growth using analyses similar to those described recently by Tvergaard and Hutchinson (2002). They analyze the growth behavior of cylindrical voids lying on the crack plane ahead of the crack tip within a small-scale yielding (SSY) boundary layer model with zero T-stress. The discrete voids have a spacing, D, along the crack plane of the SSY model within a highly

refined crack-front region. They describe computational studies focused on the growth histories of the leading voids nearest the crack front. Their study identifies both single void growth and multiple void growth mechanisms governed primarily by the initial void porosity, f_0. The crack grows in their model by release of nodal reactions (enforcing zero displacement) along the ligament (symmetry plane) between the voids. The crack extension occurs when the ligament length between voids reduces to a specified critical size. This process grows the crack in discrete increments of size equal to the length of one void ligament. Continued external loading reduces subsequent ligaments to critical length with crack extensions through additional node releases. The external loads (remotely applied K) at the point of each crack extension define the crack growth resistance (K_R and J_R) curves. Here, we employ a modified criterion for ductile crack growth where each void must obtain a critical porosity, f_c, to trigger the ligament release. This enables comparison of resistance curves obtained from discrete void models with conventional J_R–Δa curves obtained using computational cell analyses.

The work by Tvergaard and Hutchinson (2002) focuses on void growth behavior and the features of ductile crack growth initiation. They do not examine the potential effects that discrete voids may impose on cleavage fracture processes in the mid-to-upper region of the DBT. The analyses by Isacsson et al. (1998) do investigate these effects through an analysis of a single spherical void located within a unit cell. They provide "correction" factors to adjust failure probabilities based on isolated computational cells, to the higher failure probabilities caused by the otherwise neglected stress concentrations near the discrete voids. Similar to Isacsson et al. (1998), we also employ the Weibull stress model to quantify the stress concentration effects on the probability of cleavage fracture. In addition, our analyses adopt the framework developed by Tvergaard and Hutchinson (2002) to examine the effects of multiple interacting voids and small amounts of ductile crack growth. Highly refined finite element models enable the development of a non-dimensional function, $h(\widehat{J})$, to represent the stress concentration effects on the Weibull stress in a convenient framework. Here, $\widehat{J} = J/D\sigma_0$ denotes a non-dimensional loading parameter for the SSY analyses. The h-function follows from a comparison of the Weibull stress values for $f_0 > 0$ and $f_0 = 0$, i.e., $h(\widehat{J})$ quantifies the effects of discrete voids on the Weibull stress as a function of external loading,

$$\sigma_w^{f_0>0}/\sigma_w^{f_0=0} = h(J/D\sigma_0, T_\sigma/\sigma_0, f_0, f_c, m, E/\sigma_0, n, v). \tag{1}$$

These functions also reflect the increase in volume of material sampled as the crack grows from the original tip to the first void, the second void, etc. The correction function permits adjustments to the Weibull stress values computed from simple analyses which neglect the stress concentrations. The h-functions vary with material flow properties, initial porosity (f_0), critical porosity (f_c), Weibull modulus (m), and T-stress (T_σ).

The organization of this paper is as follows. Section 2 reviews very briefly the Weibull stress framework. Section 3 describes the evolution of Weibull stress values under SSY conditions and includes the effects of both discrete void stress concentrations and ductile tearing on the Weibull stress. Section 4 summarizes the finite element procedures and the numerical models adopted throughout this work. Section 5 describes the void growth history and ductile crack growth results. Section 6 presents key results of the analyses to quantify the effects of discrete voids and ductile tearing on the Weibull stress values and the corresponding cumulative failure probabilities. Section 7 concludes this paper with a short summary.

2. Weibull stress framework

Experimental testing of ferritic steels over the low-to-mid region of the DBT curve generates macroscopic fracture toughness values (K_{J_c}, J_c) that exhibit large amounts of scatter (Wallin, 1984). Weakest link models postulate that the macroscopic cleavage fracture event depends on the failure of a single initiator (Lin et al., 1986; Wallin, 1984; Wallin et al., 1984). The random distribution of initiators contributes directly to the observed scatter in experimental fracture toughness values. The volume of highly stressed

material along the crack front thus plays a key role in the fracture process. The Beremin group (1983) introduced a local fracture parameter, the Weibull stress (σ_w), to define a probabilistic scalar measure of crack-front conditions. The expression for the global cumulative probability of cleavage fracture (Beremin, 1983; Ruggieri and Dodds, 1996a; Gao and Dodds, 2000) follows as,

$$P_f(\sigma_w) = 1 - \exp\left[-\frac{1}{V_0}\int_V \left(\frac{\sigma_1}{\sigma_u}\right)^m dV\right] = 1 - \exp\left[-\left(\frac{\sigma_w}{\sigma_u}\right)^m\right], \tag{2}$$

where the scalar Weibull stress, σ_w, is given by,

$$\sigma_w = \left[\frac{1}{V_0}\int_V \sigma_1^m \, dV\right]^{1/m}. \tag{3}$$

The Weibull modulus, m, depends on the postulated shape of the probability density function for pre-existing microcracks at metallurgical inclusions (initiators). The value of m quantifies the degree of "scatter" reflected in the cumulative failure probability distribution. The scale parameter, σ_u, denotes the Weibull stress value for a cumulative probability of fracture equal to 0.63, $P_f(\sigma_w = \sigma_u) = 0.63$. Computation of the Weibull stress follows by integrating the maximum principal stress, σ_1, over the fracture process zone, V. This zone consists of the region of plastically deformed crack-front material over which the maximum principal stress exceeds a multiple (λ) of the yield strength $\sigma_1 \geqslant \lambda\sigma_0$.

In previous work, researchers generally assume that $\lambda \approx 2$, i.e., the material must be yielded and the stress must reach a sufficiently high level to initiate fracture. Weibull stress values do vary with the choice of λ, especially for low m values, e.g., $m < 12$ (see Appendix of Petti and Dodds (2004) for additional discussion). The Weibull stress definition also includes a normalizing reference volume, V_0, that provides dimensional consistency as well as another length-scale associated loosely with the microstructural features of a material related to the cleavage process (e.g. grain size). The specific value of V_0 plays a key role in applications of the Weibull stress model to predict actual values of the macroscopic fracture toughness using metallurgical scale features which govern m and σ_u. However, in applications to understand the effects of constraint loss, for example, across different cracked specimens of the same material, V_0 (as a "material" property) presumably retains the same value in each case and thus cancels in comparisons of relative Weibull stress values and relative failure probabilities. Such studies often specify a unit value of V_0 for convenience (Ruggieri and Dodds, 1996a,b).

Numerical computation of the Weibull stress given by Eq. (3) employs standard element-by-element integration techniques using finite element analyses (see Ruggieri and Dodds (1998) for additional details). The non-linear finite element model provides the continuum stress strain field in the absence of any localized, discrete features related to the cleavage triggering event, for example, the stress concentration caused by a sharp microcrack on the order of a few microns in size. Consequently, there exists no correlation between the size of the finite elements near the crack tip or voids with the value employed for V_0 or with any other microstructural length-scale for cleavage (e.g., cracked inclusion size, shape, orientation, spacing, etc.). The calibrated values of m and σ_u reflect these microstructure details in the adopted Weibull stress framework. More specifically, stress fields are not averaged over a prescribed V_0 for the computation of σ_w. The finite element solution should provide a mesh invariant, converged value for the integral in Eq. (3) including voids, which is then scaled by a calibrated value of V_0 when necessary in the application as noted above.

At a given level of external loading (J or K_J), the Weibull stress can be computed with or without a "history" effect caused by crack-front blunting and crack growth. Computations employing this history effect use the maximum stress experienced by each material point up to and including the current external load level. To neglect the history effect, computation of the Weibull stress at each level of loading uses only the current stresses. For analyses without ductile crack growth, only small differences develop between Weibull stress values for these two methods—the differences stem from the partial unloading of material behind the

current position of the peak stress ahead of the blunting crack tip. Use of the maximum stress levels experienced over the loading history increases the Weibull stress (<1%) over values computed using the current stresses. Because the Weibull stress increases rapidly with loading for high constraint conditions (SSY conditions or deep-notch C(T) and SE(B) specimens), only minimal differences in failure probability develop from including or neglecting the history effect. The history effect becomes more pronounced for low constraint conditions, i.e., shallow-notch SE(B) specimens and other negative T-stress geometries. This stems from the sensitivity of the external loading associated with a given Weibull stress value (i.e., failure probability) for shallow Weibull stress vs. load trajectories.

Small amounts of ductile crack growth lead to the sampling of additional material volume at high stress levels at the crack front. Material previously ahead of the crack front now resides behind the front and experiences inelastic unloading. The Weibull stress values increase steadily with continued loading and growth when the history effect includes the maximum stresses experienced by the (now) unloaded material behind the current crack front. In contrast, Weibull stress values computed with the current stresses increase as well, but not at the same rate. Here we use the maximum stresses and thus reflect history effects to remain consistent with the concept of a cumulative failure probability. Consider the behavior at loading levels corresponding to steady-state (or near steady-state) crack growth (i.e., a flat, crack growth resistance curve) in the SSY framework. The plastic zone does not increase further in size—it merely pushes forward along the crack plane as the crack continues to grow with little or essentially no additional loading. With no increase in the size of the plastic zone, the Weibull stress remains constant when computed with the current stresses (no history effect). This implies an associated cumulative failure probability that does not increase with subsequent ductile crack growth, i.e., the additional volume of material loaded to high stress levels during ductile growth does not increase the cumulative cleavage failure probability since an equal amount of material leaves the process zone. Conversely, use of the maximum stresses experienced by the unloaded material leads to a continual increase of the Weibull stress with crack growth. The cumulative probability for cleavage fracture $\rightarrow 1.0$ in steady growth given the increasingly large volume of material sampled at high crack-front stress levels. Use of this model assumes that failure by cleavage fracture remains possible at the analyzed temperature, i.e., the temperature of interest does not reside on the upper shelf where cleavage fracture cannot intervene regardless of the amount of sampled material.

Alternate definitions for the Weibull stress have been proposed to incorporate experimental observations which show a threshold loading below which the probability of fracture remains zero. One such proposal introduces a threshold value of the principal tensile stress, σ_{th}, into the Weibull stress definition in Eq. (3) (Bakker and Koers, 1991; Ruggieri, 2001), i.e., the integrand in Eq. (3) becomes $\sigma_1 - \sigma_{\text{th}}$. Calibration of the σ_{th} value for a specific material remains problematic. Previous work (Gao and Dodds, 2000; Petti and Dodds, 2004, 2005) addresses this issue by introducing a threshold (minimum) Weibull stress value, $\sigma_{w\text{-min}}$, into the cumulative fracture probability given by Eq. (2). Still other proposed modifications have introduced plastic strain effects on the microcrack distribution (Kroon, 2001) and temperature/loading rate dependent Weibull parameters (Petti and Dodds, 2004; Petti and Dodds, 2005). The present work employs the simple two-parameter, Weibull stress definition in Eq. (3) given the exploratory nature of the study.

3. Discrete void and ductile tearing effects on σ_w

Plane-strain, SSY conditions produce self-similar fields with amplitudes dependent only on J, or equivalently $K_J = \sqrt{EJ/(1-\nu^2)}$. This leads to the following relationship (Gao and Dodds, 2000; Lei et al., 1998) coupling the local crack-front conditions quantified by the Weibull stress with a macroscopic measure of the far-field loading, J (or K_J), i.e.,

$$\sigma_w^m = \mathscr{C} B J^2, \tag{4}$$

where B and $\mathscr{C}$ denote the thickness (i.e. crack-front length) and a material dependent constant, respectively. For plane-strain conditions, the stress field and the local J value remain constant at all points along the crack front. The material constant ($\mathscr{C}$) depends upon the flow properties ($E/\sigma_0, v, n$), Weibull parameters (m, V_0), and the specified level of T-stress (a high constraint reference condition with $T_\sigma = 0$ is most commonly adopted). For a model without voids and without ductile tearing, use of the maximum stresses to compute the Weibull stress leads to a slight increase of $\mathscr{C}$ over the loading history ($\leqslant 1\%$, depending on m). After the determination of $\mathscr{C}$ for a specific material, temperature, and loading rate, Weibull stress values follow simply from Eq. (4) for any crack-front length (B). In addition to plane-strain SSY conditions, the expression in Eq. (4) remains approximately valid for real, through-crack specimens early in the loading while SSY, $T_\sigma \geqslant 0$ conditions prevail along with uniform J over the crack front.

Gao and Dodds (2000) introduced a non-dimensional constraint function, $g(M)$, to characterize the level of constraint loss as SSY conditions gradually degrade in specimens under increased plastic deformation. The extension of Eq. (4) follows as

$$\sigma_w^m = \mathscr{C} B J_{\text{avg}}^2 g(M), \tag{5}$$

where $M = b\sigma_0/J_{\text{avg}}$ and J_{avg} denotes a through-thickness average value. The constraint function, $g(M)$, equals 1.0 for all materials under plane-strain SSY conditions with constant $T_\sigma = 0$. For a specific configuration, e.g. SE(B) with $W = 2B$ and $a/W = 0.5$, 3D non-linear finite element analyses and Weibull stress computations define σ_w as a function of J_{avg}. With the plane-strain, SSY analyses to compute $\mathscr{C}$ (for a specific material and m value), the g-function value (with respect to M) follows by solving Eq. (5) for $g(M)$ at each loading level.

Similar to the non-dimensional constraint function, $g(M)$, the proposed function, $h(\widehat{J})$, captures the coupled effects of stress concentrations near discrete voids populating the crack-front region and the additional volume of material sampled during ductile crack growth. With the assumption of $T_\sigma = 0$ under SSY conditions such that $g(M) \equiv 1$, the extension of Eq. (4) follows as,

$$\sigma_w^m = \mathscr{C} B J^2 h(\widehat{J}), \tag{6}$$

where $\widehat{J} = J/D\sigma_0$ denotes a non-dimensional loading parameter for SSY conditions with D equal to the (mean) spacing between the discrete voids. The h-functions vary with material flow properties, initial porosity (f_0), critical porosity (f_c), Weibull modulus (m), and T-stress.

For fracture specimens, the coupling of constraint loss, stress concentrations from discrete voids, and ductile crack growth all influence the Weibull stress. It seems plausible that Eqs. (5) and (6) may be combined as

$$\sigma_w^m = \mathscr{C} B J^2 h(\widehat{J}) g(\widehat{J}), \tag{7}$$

where g now becomes a function of $\widehat{J}$ to remain consistent with $h(\widehat{J})$. Alternatively, both g and h can be defined as functions of M for fracture specimens. Computation of $\mathscr{C}$ and $g(\widehat{J})$ follows from standard plane-strain, SSY and fracture specimen analyses (without discrete voids). The h-function follows from Eq. (7) using σ_w vs. J_{avg} results from the analysis of a fracture specimen which includes discrete voids. When used as the loading term in Eq. (2), values of the h and g functions other than 1.0 readily influence the failure probability. Since we only examine plane-strain, SSY conditions in this study, M cannot be employed (no ligament size, b, exists).

4. Computational procedures and models

Non-linear finite element analyses are performed on highly detailed meshes using the research code WARP3D (Koppenhoefer et al., 2001). These analyses use a standard Mises constitutive model with J_2 flow

theory including the effects of large displacements and finite strains. The uniaxial, stress–strain relationship has an initially linear region, followed by a power-law hardening region,

$$\frac{\varepsilon}{\varepsilon_0} = \frac{\sigma}{\sigma_0} \text{ for } \varepsilon \leqslant \varepsilon_0; \quad \frac{\varepsilon}{\varepsilon_0} = \left(\frac{\sigma}{\sigma_0}\right)^n \text{ for } \varepsilon > \varepsilon_0, \tag{8}$$

where σ_0, ε_0 and n denote the yield stress, yield strain and strain hardening exponent, respectively. Each finite element model consists of standard three-dimensional 8-node elements with $2 \times 2 \times 2$ Gauss quadrature. A domain integral procedure (Moran and Shih, 1987) computes J-integral values to insure agreement with K-values imposed on the remote boundary.

4.1. Conventional plane-strain SSY model

This study employs a boundary layer model (Larsson and Carlsson, 1973; Rice, 1968) wherein the plastic zone remains small compared to the radius of the outer boundary. The finite element mesh shown in Fig. 1a contains approximately 2800 elements with one element layer through the thickness. The setting of $w = 0$ at all model nodes enforces the plane-strain condition. Nodal displacements that follow a prescribed Mode I and T-stress field applied to the outer boundary serve to load the model (Anderson, 1995).

$$u(R,\theta) = \frac{K_I(1+\nu)}{E}\sqrt{\frac{R}{2\pi}}\cos\left(\frac{\theta}{2}\right)(3-4\nu-\cos\theta) + T_\sigma\frac{(1-\nu^2)}{E}R\cos\theta, \tag{9}$$

$$v(R,\theta) = \frac{K_I(1+\nu)}{E}\sqrt{\frac{R}{2\pi}}\sin\left(\frac{\theta}{2}\right)(3-4\nu-\cos\theta) - T_0\frac{\nu(1+\nu)}{E}R\sin\theta. \tag{10}$$

Fig. 1b illustrates the detailed crack-tip region of the SSY mesh with initial root radius 2.5 μm. Use of a very small, initial root radius aids in convergence of the finite-strain analyses.

4.2. Plane-strain SSY model with discrete voids

Fig. 2 shows the introduction of discrete voids into the plane-strain SSY model following the same approach used by Tvergaard and Hutchinson (2002). The present model neglects the void nucleation process and includes the voids at the onset of loading. The initially cylindrical voids have prescribed uniform spacing, D, along the crack plane. The initial radius of the voids, r_0, together with D, lead to initial void volume ratios or porosity given by $f_0 = \pi(r_0/D)^2$. Here we analyze f_0 values of 0.001, 0.0021, 0.0035 and 0.0055 to span the transition from a single void growth mechanism (i.e., void by void growth) to multiple void growth

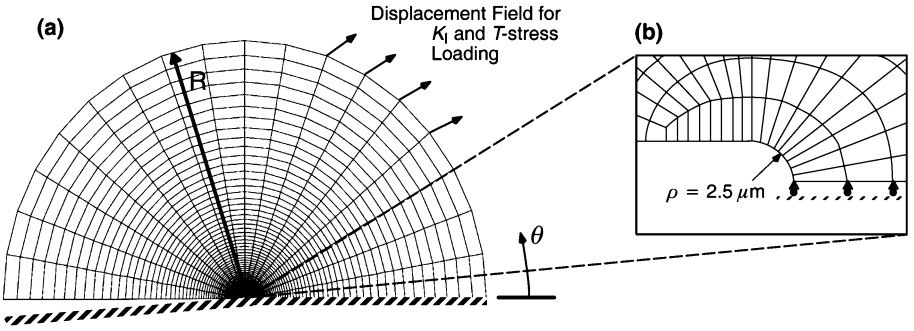

Fig. 1. (a) Small-scale yielding (SSY) mesh for plane-strain analyses, and (b) the crack-tip region.

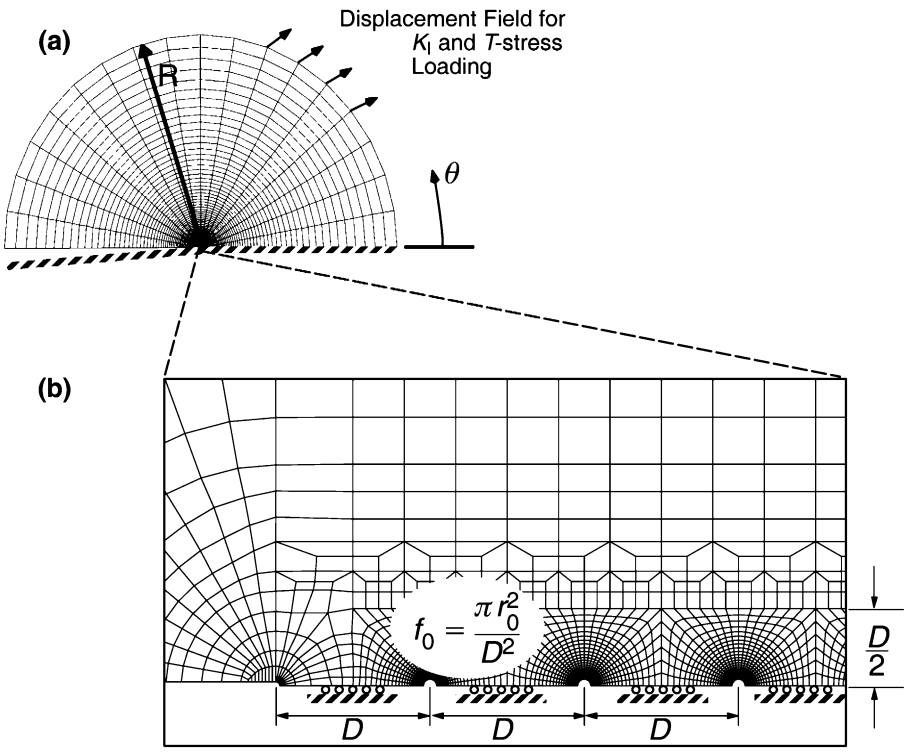

Fig. 2. (a) Small-scale yielding (SSY) mesh for plane-strain analyses, and (b) the crack-tip region with cylindrical, discrete voids at spacing, D, along the crack plane.

mechanisms. Tvergaard and Hutchinson (2002) found that for an $E/\sigma_0 = 333$, $n = 10$ material with relatively small f_0 values near 0.001, significant expansion occurs only in the first void (nearest the crack tip). Larger f_0 values of 0.0035, for example, lead to significant expansion in multiple voids even at low load levels.

The void spacing, D, and initial root radius at the crack tip, ρ_0, remain constant at 100 μm and 2.5 μm, respectively, for all values of f_0. The highly refined meshes around the discrete voids lead to finite element models containing 25,000–28,000 elements (with one element layer through the thickness). Meshes with this level of refinement appear necessary to resolve the stress gradients in the voided region. This computational model clearly reflects a highly idealized microstructure associated with the notion of pre-existing voids (cylindrical shapes, uniform spacing, uniform f_0, etc.). The exploratory nature of this study does not warrant, for example, models with random spacing of the voids.

The finite element model does not reflect any discrete features or length-scales of the microstructure associated with the inclusions, often much smaller than the voids, that trigger the cleavage fracture process (inclusion size, shape, strength, orientation; or the grain size, shape, strength, orientation). Rather, we adopt the stochastic concepts and associated parameters (m, σ_u, V_0) of the Beremin model to represent the cleavage mechanism driven by the stress field present in a "smeared" continuum. The finite element model here provides a high quality, continuum solution for a well-posed, non-linear boundary value problem of a domain containing initially smooth voids undergoing (large) elastic–plastic deformations and without loss of stress carrying capacity (no damage) of intact material between the discrete voids. Convergence of the continuum solution with Mode I crack growth by node release and with non-softening constitutive models does not require the specification of an internal length-scale. The interpretation of our

computational results in the context of the microstructures for a specific steel does require some care. The present results, for example, appear most applicable to older pressure vessel steels having larger inclusions (e.g. MnS) that drive the void growth prior to a cleavage event triggered by much smaller (carbide) inclusions.

Crack growth initiates in the analyses when the void nearest to the crack tip reaches a critical size or porosity, f_c. The very high levels of mesh distortion near the leading voids limit consideration of f_c to the range of 0.05–0.08 in these computations. When the void nearest the crack tip reaches f_c, the constraints applied to nodes along the ligament between the crack tip and first void are removed, with the nodal tractions reduced to zero over 800 load steps without additional external loading. Numerical stability requires this large number of load steps to remove the tractions—Tvergaard and Hutchinson (2002) encountered this same difficulty. The crack grows by one void spacing, $\Delta a = D$, after release of the first ligament. The remote loading then increases until the second void reaches f_c, which triggers release of the second ligament. This process continues until excessive element distortion around the discrete voids prevents further analysis, or when the additional remote loading (ΔK) required to grow the next void to f_c decreases to zero, i.e., the crack growth resistance (J_R–Δa) curve becomes flat.

Tvergaard and Hutchinson (2002) use the ratio of the deformed ligament length to the original ligament length as the criterion to initiate or continue crack growth. Rice and Johnson (1970) and McMeeking (1977) previously employed this criterion. Our study employs attainment of a critical porosity, f_c. This permits direct comparison with J_R–Δa curves computed by traditional computational cell (Gurson–Tvergaard) models which generally employ a critical porosity criterion for crack growth through element extinction. The present calculations with the discrete void model reveal the same variety of mechanisms, single void and multi-void growth, observed by Tvergaard and Hutchinson (2002). However, the focus here lies on the effects of the growing voids, the resulting stress concentrations, and the ductile crack growth on the Weibull stress and thus the cumulative failure probability.

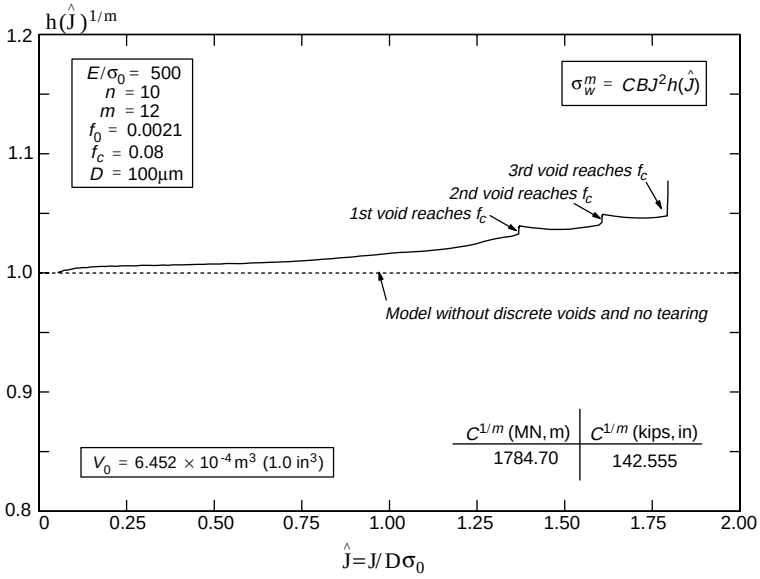

Fig. 3. Non-dimensional h-function for a moderately hardening material, $E/\sigma_0 = 500$, $n = 10$, with initial porosity, $f_0 = 0.0021$, critical porosity, $f_c = 0.08$, and Weibull modulus, $m = 12$.

Fig. 3 illustrates an h-function for a moderate hardening material ($E/\sigma_0 = 500$, $n = 10$) with an initial void porosity (f_0) of 0.0021, critical porosity (f_c) equal to 0.08, void spacing (D) of 100 μm, and Weibull modulus (m) of 12 (plotted as $h^{1/m}$ to show the stress concentration and ductile crack growth effect on σ_w and not σ_w^m). Void growth with no crack extension occurs over a normalized loading, $J/D\sigma_0$, $0 \rightarrow 1.35$. In this region, $h^{1/m}$ increases above unity due only to the effects of stress concentrations near the discrete voids. The ridges in the curve at $J/D\sigma_0 \approx 1.35$, 1.6 and 1.8 correspond to growth from the initial crack tip to the first void, from the first void to the second void, and from the second void to the third void, respectively. Once crack growth occurs, part of the increased Weibull stress (reflected through the h-function) stems from the increased volume of sampled material. Section 6 provides a detailed discussion of h-functions for various values of the initial and critical porosities.

4.3. Plane-strain SSY model with computational cells

The discrete model for void growth incurs significant computational cost but does provide details of stress–strain fields near the voids. Less detailed and less computationally demanding continuum representations of softening due to void growth have been used extensively, most recently cast into a "computational cell" framework (Xia and Shih, 1996; Broberg, 1994). The Weibull stress values from such models include the effects of smeared voids on the local stress field and the additional material volume sampled as the crack advances, but not the local stress concentration effects of the voids. The SSY model shown in Fig. 4 replaces the detailed representation of discrete voids with computational cells placed along the crack plane (Xia and Shih, 1996). In the present use of this model, each cell consists of a single finite element with a Gurson–Tvergaard (GT) (Gurson, 1977; Tvergaard, 1990) constitutive model to describe the continuum damage from void growth. The initial void volume fraction, f_0, for each computational cell increases with deformation eventually leading to a gradual loss of stress capacity. The yield function for the GT model is given by

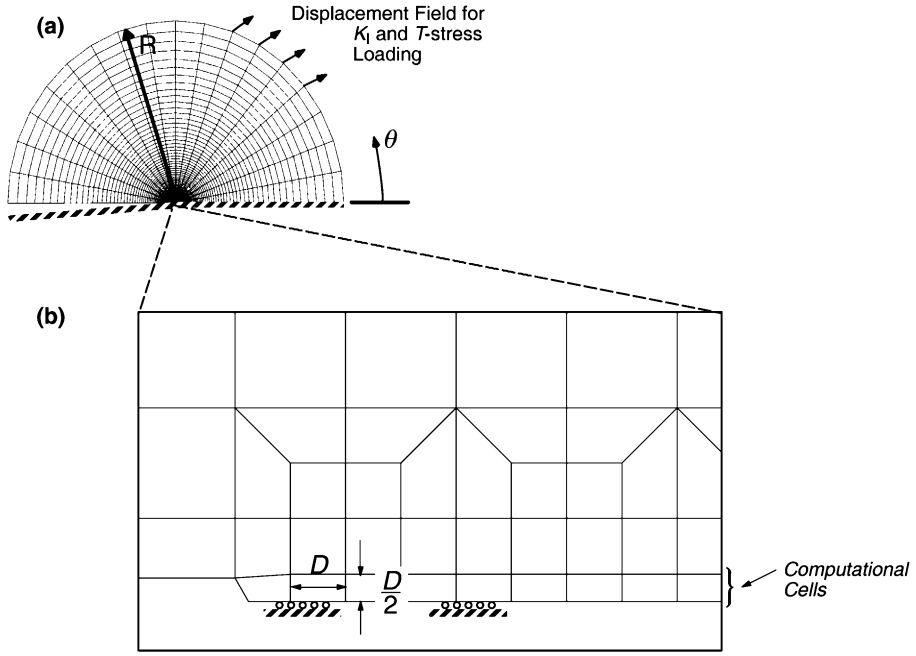

Fig. 4. (a) Small-scale yielding (SSY) mesh for plane-strain analyses, and (b) the crack-tip region with computational cell elements placed along the crack plane.

$$\phi(\sigma_e, \sigma_m, \bar{\sigma}, f) = \left(\frac{\sigma_e}{\bar{\sigma}}\right)^2 + 2q_1 f \cosh\left(\frac{3q_2\sigma_m}{2\bar{\sigma}}\right) - \left(1 + q_1^2 f^2\right) = 0, \tag{11}$$

where σ_e denotes the Mises equivalent macroscopic stress, σ_m, the mean macroscopic stress, $\bar{\sigma}$, the Mises equivalent stress of the matrix material, and f, the current void volume fraction or porosity. To provide direct comparison with J_R–Δa curves obtained with discrete void models, we calibrate q_1 and q_2 with a simple least squares procedure to produce the same crack growth behavior of the discrete void analyses in Section 4.2. When the average value of f at the Gauss points in a cell element reaches a defined value of f_c, the stiffness of the cell element reduces to zero. The background (non-GT cell) elements have $f = 0$ and follow standard J_2 flow theory with the uniaxial stress–strain relations in Eq. (8). WARP3D (Koppenhoefer et al., 2001) implements the GT and automatic cell extinction models within a finite-strain framework (Gullerud and Dodds, 2000; Ruggieri et al., 1996).

For consistency with the discrete void analyses, the cell model analyses use a cell size of $D = 100$ μm equal to the discrete void spacing. In the symmetric model employed here, the cell has a height $D/2$ and a width equal to D. The crack growth also occurs in increments (Δa) equal to D when the solution procedures remove cells that reach $f = f_c$. The much coarser mesh of the cell element model limits the resolution of stress gradients in the crack-tip region that proves critical in the computation of Weibull stress values. This represents a major drawback of the computational cell approach within the framework to quantify void effects on cleavage fracture. Howard et al. (Bilby et al., 1994; Howard and Li, 2000) have explored a "sub-cell" approach to address this issue. This deficiency also leads to the use of gradient theories with prescribed length-scales (Tvergaard and Needleman, 1995). However, such advanced approaches introduce additional issues in the modeling (e.g., which physical quantities should be selected for the gradient averaging).

5. Resistance curves for discrete void and cell models

Fig. 5 illustrates the initial crack-front regions for the smallest ($f_0 = 0.001$) and largest ($f_0 = 0.0055$) initial void volume fractions examined in this study. This range of initial porosities captures the two mechanisms of void growth for moderate hardening materials ($n \approx 10$) in the framework of a plane-strain model having cylindrical voids. The smaller volume fraction leads to void-by-void (or single void) crack growth wherein only the void nearest to the current crack tip increases significantly in size with loading. The second void does not experience significant growth until after the crack extends beyond the first void. The model with the largest volume fraction exhibits the multiple void growth mechanism wherein multiple voids grow ahead of the current crack front.

Fig. 6 shows the deformed crack-front regions for the $f_0 = 0.001$ and 0.0055 models just prior to release of the ligament between initial crack front and the first void. In each case, the first void has attained the critical porosity (f_c) of 0.08. The $f_0 = 0.001$ analysis requires a larger external loading level, $J/D\sigma_0 = 1.55$, to reach critical porosity compared to $J/D\sigma_0 = 0.90$ for the model with $f_0 = 0.0055$. Fig. 6a and b clearly show the void-by-void (6a) and multiple void (6b) growth mechanisms. In Fig. 6b, the second void shows substantial expansion that also approaches the critical porosity. The effects on crack-tip opening displacement (CTOD) are also clearly evident as well.

Fig. 7 illustrates the deformed crack-front regions when the second void reaches critical porosity. Since only the void nearest the current crack tip increases significantly in size for the $f_0 = 0.001$ model, additional external loading to $J/D\sigma_0 = 2.1$ becomes necessary to reach the critical porosity. In this model with $f_0 = 0.001$, extensive element deformation prevents continuation of the analysis beyond $f = 0.075$ as indicated on the figure. For the $f_0 = 0.0055$ model essentially no increase in load becomes necessary to reach $f = f_c$ in the second void, i.e., the load redistribution that occurs during release of the first

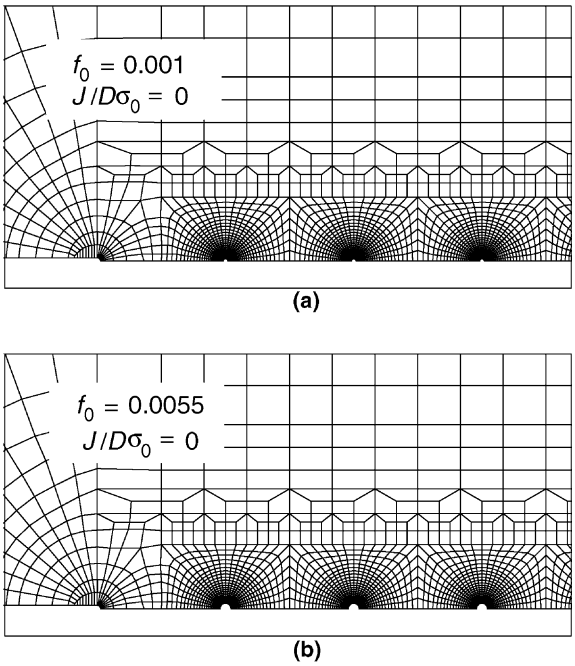

Fig. 5. Crack-tip regions for the (a) $f_0 = 0.001$ and (b) $f_0 = 0.0055$ models prior to the initiation of external loading, $J/D\sigma_0 = 0$.

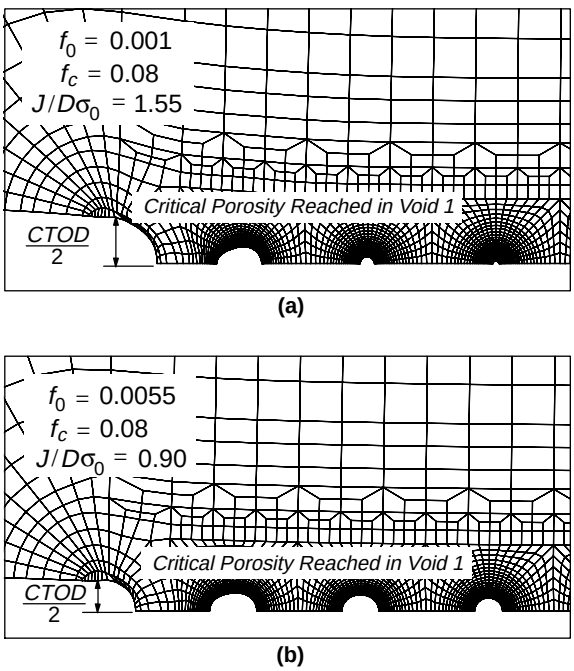

Fig. 6. Deformed crack-tip regions at true scale at critical porosity, $f_c = 0.08$, in the first void for (a) $f_0 = 0.001$ and (b) $f_0 = 0.0055$ at $J/D\sigma_0 = 1.55$ and 0.90, respectively. The background material has $E/\sigma_0 = 500$, $n = 10$.

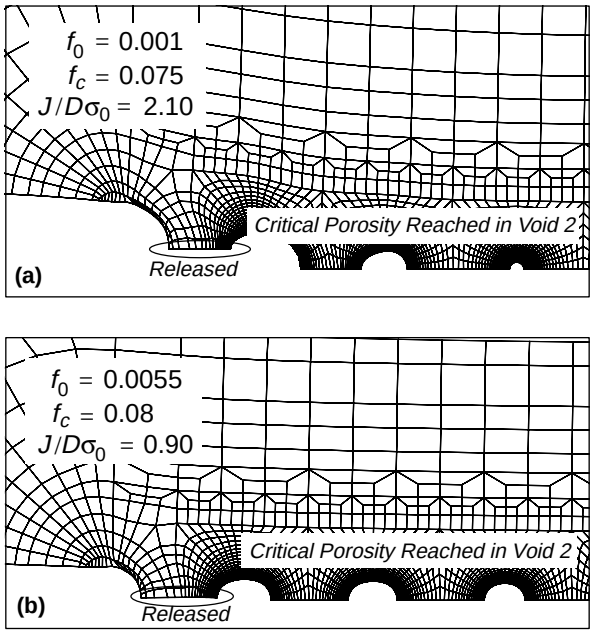

Fig. 7. Deformed crack-tip regions at true scale at critical porosity, $f_c = 0.08$, in the second void for (a) $f_0 = 0.001$ and (b) $f_0 = 0.0055$ at $J/D\sigma_0 = 2.10$ and 0.90, respectively. The background material has $E/\sigma_0 = 500$, $n = 10$ ($f_c = 0.075$ for the $f_0 = 0.001$ analysis).

ligament increases deformation at the second void to the critical value without any additional external load.

Fig. 8 summarizes the crack growth histories (J_R–Δa) for a series of analyses with discrete voids. The value of external loading, $J/D\sigma_0$, at the critical porosity in each void defines the points shown on the J_R curves. The crack grows by increments of the void spacing, D, and the J_R curves have discrete $\Delta a/D$ values

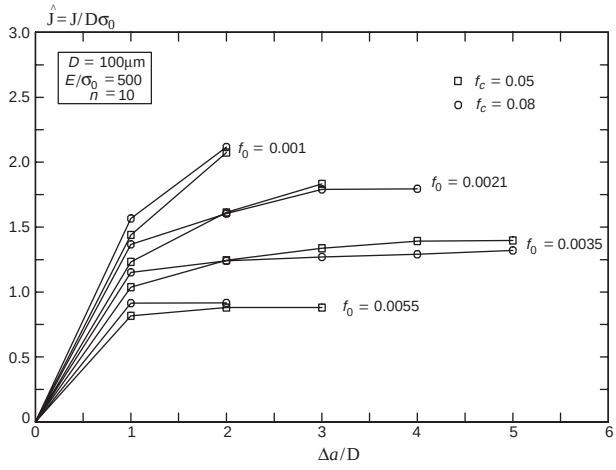

Fig. 8. Crack growth resistance curves computed with the discrete void model for a moderately hardening material ($E/\sigma_0 = 500$, $n = 10$) with initial porosities, $f_0 = 0.001$, 0.0021, 0.0035 and 0.0055, and critical porosities, $f_c = 0.05$ and 0.08. The applied T-stress = 0 for these results.

at 1.0, 2.0, 3.0, etc. Tvergaard and Hutchinson (2002) plot critical values of $J/D\sigma_0$ at $\Delta a/D = 0.5$, 1.5, 2.5, etc., corresponding to the use of a critical deformed ligament length and not the critical porosity in the voids as employed here. Fig. 8 illustrates the key features of the tearing resistance for the four initial porosities (0.001. 0.0021, 0.0035, and 0.0055) studied here. Smaller initial porosities lead to higher initiation toughness (more so for $f_c = 0.08$) and to higher resistance curves. For the larger initial porosity $f_0 = 0.0055$, the resistance curve becomes flat with little or no additional external loading after the initiation of crack growth.

Fig. 10a shows a representative J_R–Δa curve for a material with greater strain hardening and lower yield stress. Here, $f_0 = 0.0021$ with $f_c = 0.08$ for a material with flow properties $E/\sigma_0 = 800$, $n = 5$. This $E/\sigma_0 = 800$ value for $n = 5$ reflects the general trends measured for tensile properties of ferritic steels. A detailed comparison of the void growth histories for the high and moderate hardening material reveals that higher hardening suppresses growth of voids beyond the one adjacent to the current crack tip, i.e., increased hardening favors the void-by-void mechanism. The crack growth resistance curve in Fig. 10a illustrates the increased tearing resistance for higher hardening material that follows from the suppressed growth rates of voids ahead of the crack tip.

Fig. 10b illustrates the effects of a negative T-stress on the crack growth resistance curve for the moderately hardening material ($E/\sigma_0 = 500$, $n = 10$). The negative T-stress increases linearly in the analysis with the remotely applied K_I, $T_\sigma = qK_I$, where $q = -1.57/\sqrt{\text{m}}$ $(-0.25/\sqrt{\text{in}})$. Conversion of K_I to J and

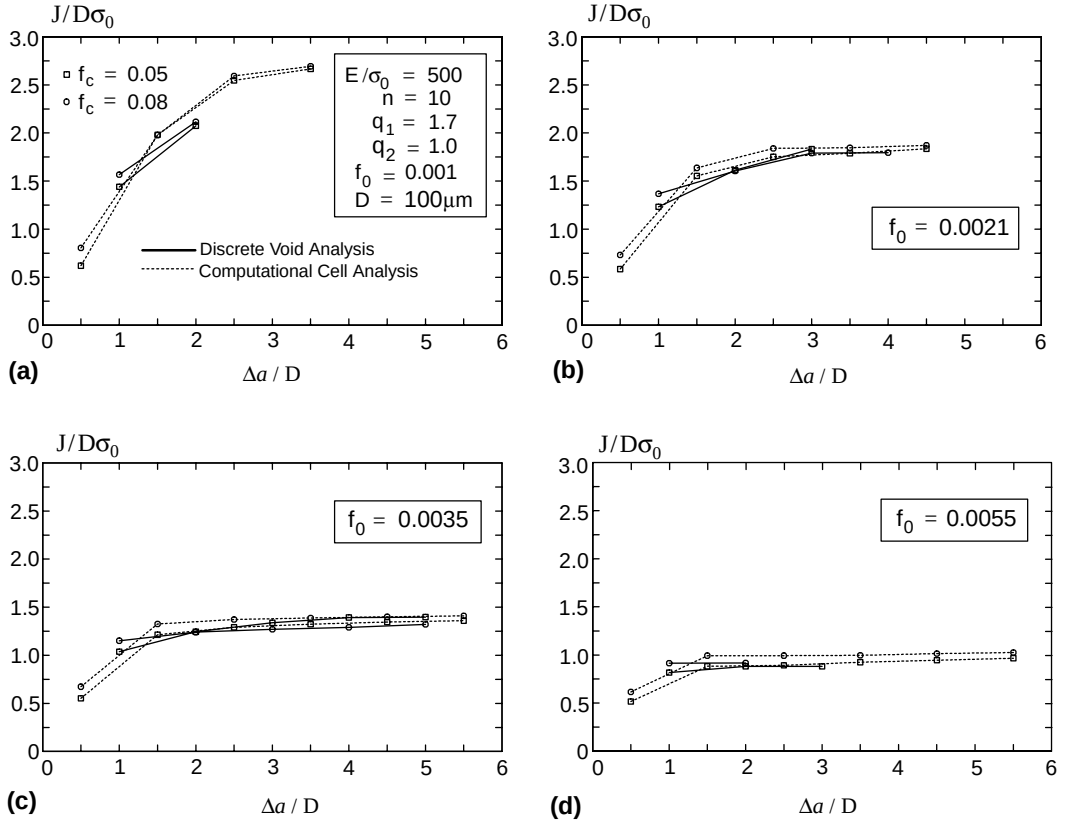

Fig. 9. Comparison of discrete void and computational cell crack growth resistance curves for $E/\sigma_0 = 500$, $n = 10$, with initial porosities: (a) $f_0 = 0.001$, (b) 0.0021, (c) 0.0035 and (d) 0.0055, and critical porosities, $f_c = 0.05$ and 0.08.

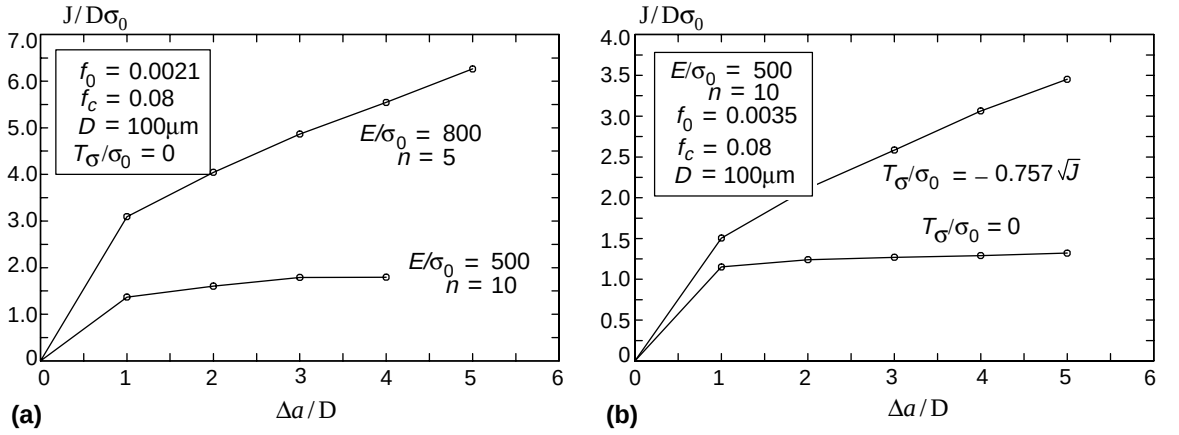

Fig. 10. Comparison of crack growth resistance curves computed with the discrete void model for (a) high ($E/\sigma_0 = 800$, $n = 5$) and moderately ($E/\sigma_0 = 500$, $n = 10$) hardening material with $f_0 = 0.0021$ and $f_c = 0.08$, and (b) negative T-stress effect with $E/\sigma_0 = 500$, $n = 10$, $f_0 = 0.0035$ and $f_c = 0.08$.

normalizing by σ_0 leads to $T_\sigma/\sigma_0 = \hat{q}\sqrt{J}$, where $\hat{q} = -0.0572\ \mathrm{m}/\sqrt{\mathrm{kJ}}$ $(-0.76\sqrt{\mathrm{in}/\mathrm{kip}})$. For this example, $\sigma_0 = 414$ MPa (60 ksi), $E = 206.9$ GPa (30,000 ksi), and $\nu = 0.3$. At the onset of ductile tearing, $T_\sigma/\sigma_0 = -0.45$, and at the last increment of growth ($\Delta a/D = 5$), $T_\sigma/\sigma_0 = -0.68$. This solution reflects an initial and critical porosity, $f_0 = 0.0035$ and $f_c = 0.08$. As expected, the negative T-stress loading decreases significantly the growth rates in the 2nd, 3rd, etc., voids ahead of the crack tip and raises the resistance curve under increased load as the T-stress becomes more negative.

Fig. 9 compares the crack growth resistance curves obtained with the discrete void models to those obtained with the computational cell models. The q_1 and q_2 parameters of the GT constitutive model, Eq. (11), have values selected to provide the overall best agreement with the discrete model for all initial porosities. Values of $q_1 = 1.7$ and $q_2 = 1.0$ provide quite good agreement for the moderate hardening material ($E/\sigma_0 = 500$, $n = 10$). For the computational cell analyses, Fig. 9 has the $J/D\sigma_0$ values plotted at the $\Delta a/D$ values corresponding to the center of each computational cell, i.e., $\Delta a/D = 0.5$ when the first cell reaches critical porosity, $\Delta a/D = 1.5$ for the second cell, etc.

6. Effects of voids and crack growth on cleavage fracture

6.1. Effects of initial and critical porosity

The effects of stress concentrations that develop around the growing discrete voids and the additional volume of material sampled at high stresses with the advancing crack both increase the Weibull stress values. This leads to an increase in the cumulative probability of fracture through Eq. (2) relative to a non-voided continuum without crack growth. The comparisons here use the non-dimensional function, $h(\widehat{J})$, from Eq. (6), to quantify the effects of stress concentrations and ductile crack growth. Figs. 11a and 12a show the increase of $h(\widehat{J})$ above 1.0 with loading for the moderate hardening material ($E/\sigma_0 = 500$, $n = 10$), two initial void porosities ($f_0 = 0.0021$ and 0.0055), and two critical porosities ($f_c = 0.05$ and 0.08) for a single Weiull modulus, m, value of 12. Prior to release of the first ligament (advance of the crack tip), the stress concentrations alone near the growing voids cause $h(\widehat{J})$ to exceed 1.0. Subsequent crack extensions through release of the intervoid ligaments lead to the vertical jumps in the

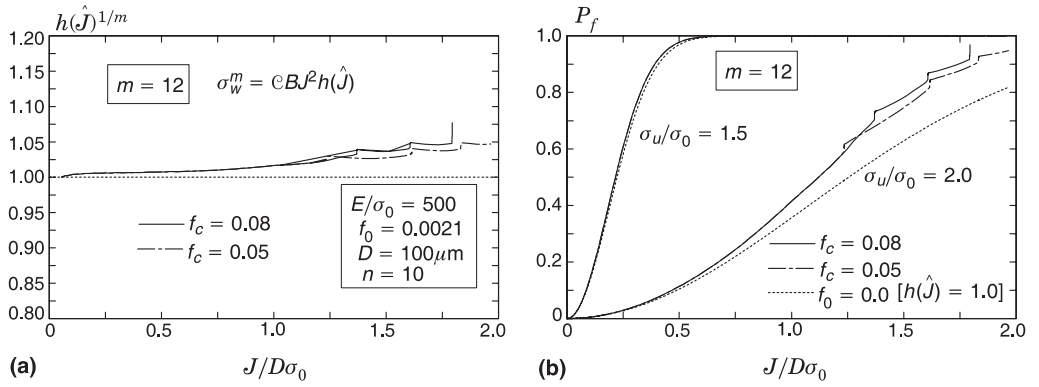

Fig. 11. (a) Non-dimensional h-function of Eq. (6) for $E/\sigma_0 = 500$, $n = 10$, $f_0 = 0.0021$, $m = 12$ for both $f_c = 0.05$ and 0.08, and (b) predictions of cumulative failure probability with specified values of $\sigma_u/\sigma_0 = 1.5$ and 2.0.

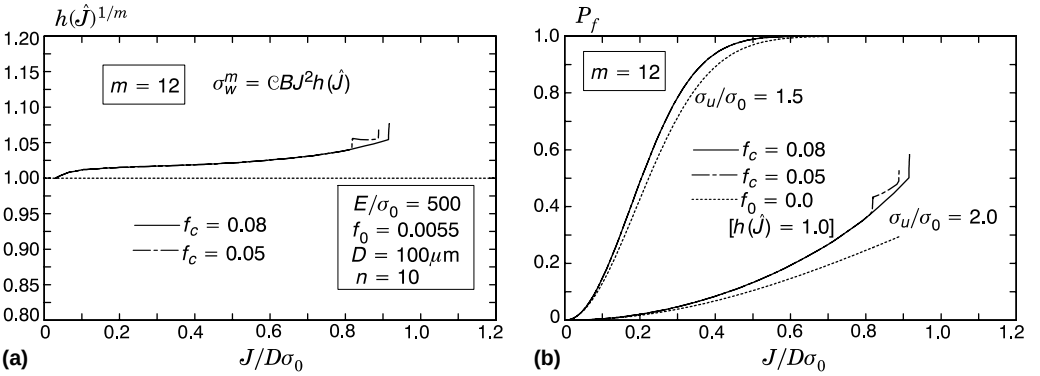

Fig. 12. (a) Non-dimensional h-function of Eq. (6) for $E/\sigma_0 = 500$, $n = 10$, $f_0 = 0.0055$, $m = 12$ for both $f_c = 0.05$ and 0.08, and (b) predictions of cumulative failure probability with specified values of $\sigma_u/\sigma_0 = 1.5$ and 2.0.

h-function curves. At the jumps, the Weibull stress increases from the additional volume of material sampled as the load shifts forward from released ligaments to the following ligaments with no increase of the external loading. Recall that the Weibull stress values here reflect prior maximum stress values in the unloaded and released ligaments.

Figs. 11b and 12b show the corresponding impact of increased Weibull stress values on the cumulative failure probability using the simple two-parameter model in Eq. (2). Construction of the plots requires numerical values for the scale parameter, σ_u ($\sigma_u = \sigma_w$ when $P_f = 0.632$). Two values are chosen to examine effects of the h-function at different levels of material toughness. The smaller value of $\sigma_u/\sigma_0 = 1.5$ represents the toughness expected at lower temperatures, i.e., the lower region of the ductile-to-brittle transition (DBT) curve. The larger value of $\sigma_u/\sigma_0 = 2.0$ corresponds to material toughness levels in the mid-to-upper regions of the DBT curve where small amounts of ductile tearing occur prior to cleavage fracture. Figs. 11b and 12b include the conventional plane-strain, SSY results without voids and growth, $h(\widehat{J}) = 1.0$, for comparison. In these comparisons, the Weibull stress scaling volume (V_0) remains at a fixed unit value. The assigned V_0 value enters the computation of Weibull stress values with and without discrete voids–crack growth in the same form through Eq. (3) and thus cancels out in the generation of h-function values, see Eq. (1).

Fig. 11 shows the h-function and examples of the cumulative failure probability for the $f_0 = 0.0021$ analyses. Over $0 \leqslant J/D\sigma_0 \leqslant 1.25$, the h-function values and cumulative failure probabilities reflect only the effects of stress concentrations prior to crack extension. For the range of external loading examined with $\sigma_u/\sigma_0 = 1.5$, $h^{1/m} \approx 1.0$ and no significant difference exists between the cumulative failure probability curves. Larger differences exist between the cumulative failure probability curves (10–15%) for $\sigma_u/\sigma_0 = 2.0$. Higher levels of external loading increase $h^{1/m}$ due to both the stress concentrations and the increase in the volume of material sampled with release of the first ligament at $J/D\sigma_0 = 1.25$ and 1.35 for $f_c = 0.05$ and 0.08, respectively, and following ligaments. Curves for the larger critical porosity ($f_c = 0.08$) lie slightly above the curves for $f_c = 0.05$. The additional external loading required to reach $f_c = 0.08$ increases the stress levels near the leading voids thereby causing slight increases in $h^{1/m}$. The vertical segments that terminate the $h^{1/m}$ and cumulative failure probability curves for the $f_c = 0.08$ analyses indicate steady crack growth, i.e., steady crack growth continues to increase the volume of material sampled with no additional external loading ($J \equiv$ constant). The analyses for $f_c = 0.05$ do not reach steady crack growth since excessive element deformation prevents the analysis from continuing past the critical porosity in the fourth void at $J/D\sigma_0 = 1.95$.

The larger initial porosity, $f_0 = 0.0055$, in Fig. 12 leads to higher values of $h^{1/m}$ and cumulative failure probabilities throughout the loading history. A small (<5%) increase in the cumulative failure probability curve exists due to the stress concentrations when $\sigma_u/\sigma_0 = 1.5$. The increase in external loading for $\sigma_u/\sigma_0 = 2.0$ shows a significant increase in failure probability (~20% compared to <5% for the $f_0 = 0.0021$ analyses) for relatively low external loading ($J/D\sigma_0 \lesssim 0.9$). This illustrates an increase in the stress concentration effect with higher initial porosity. The crack growth resistance curves reach steady crack growth after the release of the second ligament for the $f_c = 0.05$ analysis and after the release of the first ligament for the $f_c = 0.08$ analysis. After achieving steady crack growth, the $h^{1/m}$ and cumulative failure probability curves continue to increase to 1.0 with no increase in external loading.

Effects of the stress concentrations could be uncoupled from the effects of crack growth through comparison of the h-functions for computational cell analyses with the h-functions for discrete void analyses. However, concerns arise about the mesh used in the computational cell analyses (Fig. 4) since it contains relatively large ($D \times D/2$) elements along the crack plane. These large elements reduce the resolution of the stress gradients in the crack-front region. This stress field resolution proves critical in computing accurate Weibull stress values. The computed $\mathscr{C}$ constants (defines the relationship between the Weibull stress and external loading, J) derived from the computational cell model are larger than the $\mathscr{C}$ values computed with the highly refined mesh (Fig. 1). This inconsistency between the $\mathscr{C}$ constants prevents meaningful comparison with the discrete void analyses.

6.2. Effects of Weibull modulus, m, and flow properties

Figs. 13 and 14 illustrate the effects of a range of typical values for the Weibull modulus, m, on the h-function and cumulative failure probability for the $f_0 = 0.0021$, $f_c = 0.08$ analysis. Increased m values produce larger values of the Weibull stress at equivalent (remote) loading (see Eq. (3)). Larger m values also assign a greater relative "weight" to the most highly stressed regions ahead of the crack tip in computation of the total Weibull stress value. Fig. 13 shows this trend clearly both before and after the onset of crack extension. Fig. 14 shows the corresponding effects on the cumulative failure probabilities as m increases from 8 to 16. At $m = 8$, the cumulative failure probability shows almost no effects of the concentrations from void growth and crack extension. At $m = 12$ and 16, the effects become clearly significant. Note that the values of σ_u/σ_0 must increase with m—the Weibull stress magnitudes increase with the larger m values at equivalent $J/D\sigma_0$ levels.

Fig. 15 shows the effects of a higher hardening material ($E/\sigma_0 = 800$, $n = 5$) on the h-function and cumulative failure probability values for $f_0 = 0.0021$ and $f_c = 0.08$. The h values show a gradual increase with

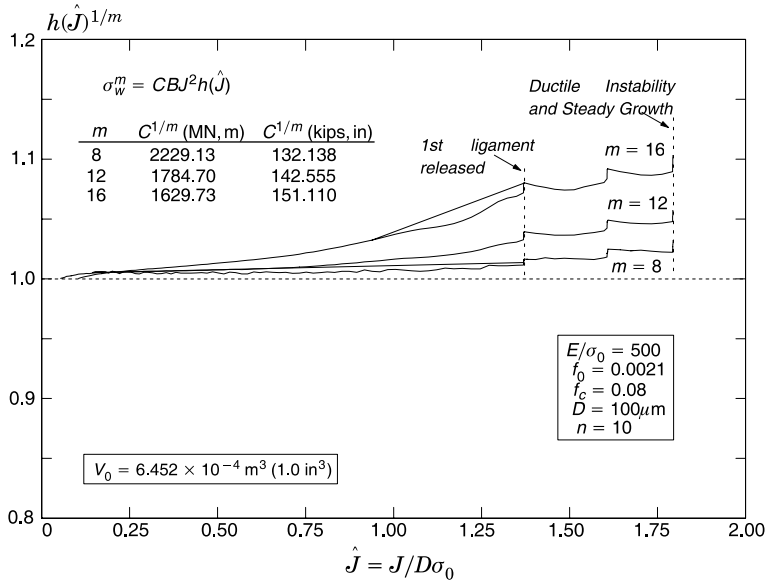

Fig. 13. Effects of Weibull modulus (m) on the non-dimensional h-function of Eq. (6) for the moderately hardening material, $E/\sigma_0 = 500$, $n = 10$, with $f_0 = 0.0021$ and $f_c = 0.08$.

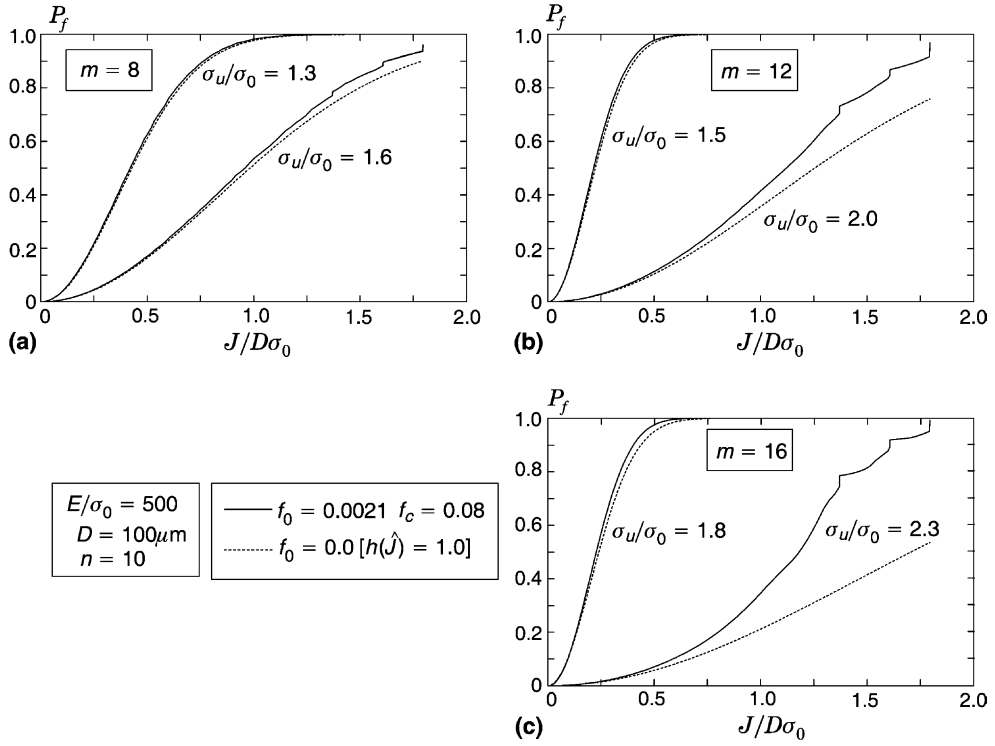

Fig. 14. Effects of Weibull modulus (m) on the predictions of cumulative failure probabilities for the moderately hardening material, $E/\sigma_0 = 500$, $n = 10$, with $f_0 = 0.0021$ and $f_c = 0.08$ for (a) $m = 8$, (b) $m = 12$, and (c) $m = 16$.

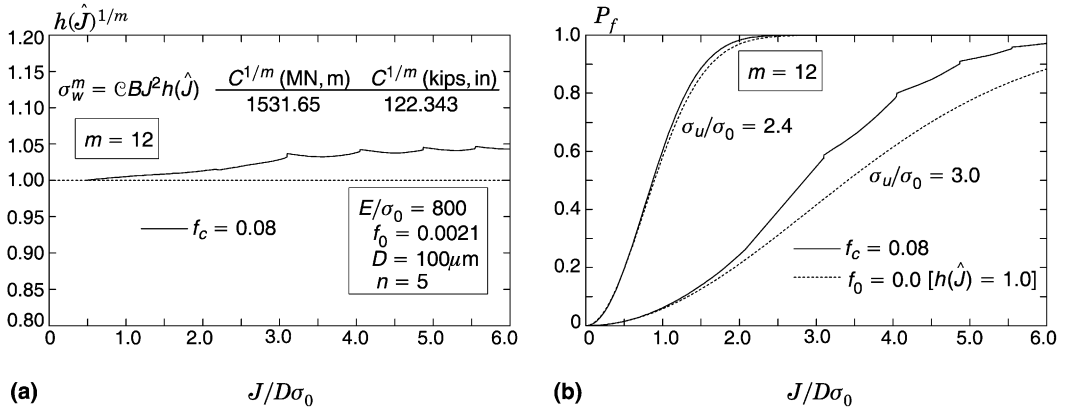

Fig. 15. (a) Non-dimensional h-function for a high hardening material ($E/\sigma_0 = 800$, $n = 5$), $f_0 = 0.0021$, $f_c = 0.08$, and $m = 12$, and (b) predictions of cumulative failure probability for $\sigma_u/\sigma_0 = 2.4$ and 3.0.

loading prior to release of the first ligament at $J/D\sigma_0 = 3.1$. This trend continues during subsequent increases of load and additional ligament releases. The relatively smooth response (compared to Fig. 11 for the $n = 10$ material) reflects the single void growth mechanism of this high hardening material. Rapid increases of h values occur in the cases of multiple void growth mechanism (i.e. low resistance curves).

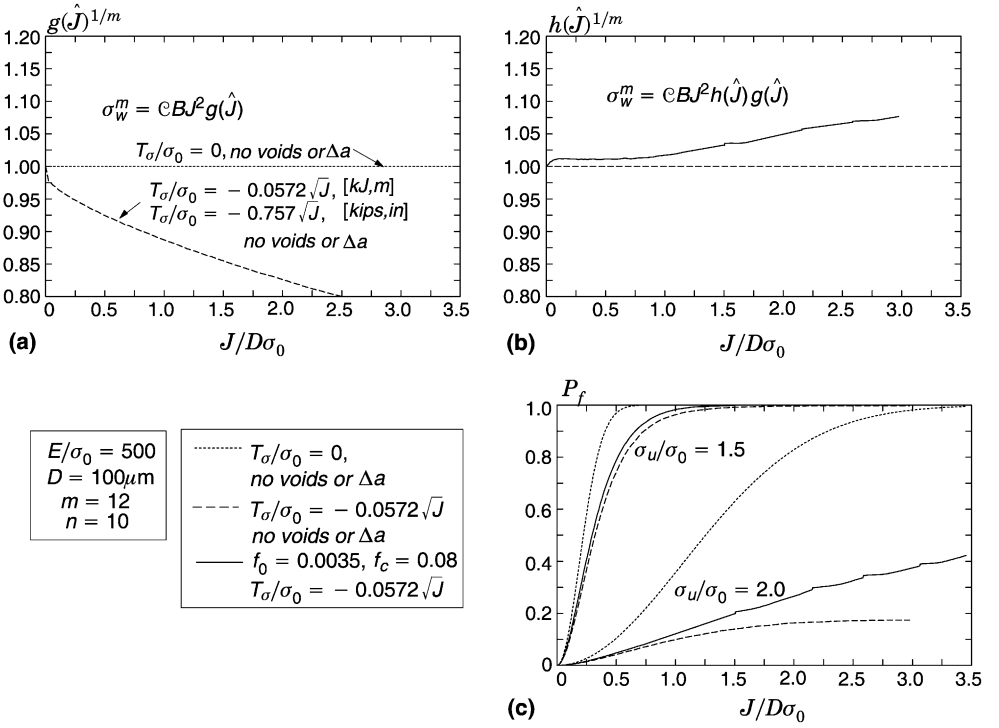

Fig. 16. Effects of negative T-stress on (a) non-dimensional g-function (constraint) and (b) non-dimensional h-function for $E/\sigma_0 = 500$, $n = 10$, $f_0 = 0.0021$, $f_c = 0.08$, and $m = 12$, and (c) predictions of cumulative failure probability with $\sigma_u/\sigma_0 = 1.5$ and 2.0.

6.3. Effects of non-zero T-stress

Application of a negative T-stress in the SSY model simulates a low constraint fracture specimen (shallow-notch SE(B), M(T), etc.). The analysis here examines $f_0 = 0.0035$ and $f_c = 0.08$ for the moderate hardening material ($E/\sigma_0 = 500$, $n = 10$). The specified negative T-stress increases linearly with applied K_I (T-stress increases with $\sqrt{J}$, $T_\sigma/\sigma_0 = -0.0572\sqrt{J}$).

The constant, $\mathscr{C}$, is first computed with Eq. (4) using the standard SSY, $T_\sigma = 0$, model shown in Fig. 1 without discrete voids. By repeating the SSY analysis using the same model and now with the applied negative T-stress, the g-function follows from Eq. (5) to describe the effect of the negative T-stress on the Weibull stress values. Fig. 16a shows clearly the significant reduction in the g-function (and thus σ_w) caused by the negative T-stress. The negative T-stress and resulting reduction in the Weibull stress values (long dash curves) lead to a significant drop (~25%) in the cumulative failure probability compared to the $T_\sigma = 0$, $g(\widehat{J}) = 1$, analysis (short dash curves) even at low σ_w/σ_0 values (see Fig. 16c).

With $\mathscr{C}$ and $g(\widehat{J})$ known, the h-function values follow from Eq. (7) and the computed Weibull stress values from the corresponding analysis with discrete voids. The introduction of discrete voids and the resulting stress concentrations in the negative T-stress analysis increases the Weibull stress over the analysis without discrete voids, as indicated in Fig. 16b when $h(\widehat{J}) > 1$. At low values of σ_w/σ_0, stress concentrations from the discrete voids increase slightly (~4%) the cumulative failure probability over the negative T-stress analysis without voids. While at high values of σ_w/σ_0, the cumulative failure probability increases significantly (>20%) in the presence of discrete voids and ductile crack growth.

7. Summary

The following key points summarize the results of this study:

- Initial porosities, f_0, ranging from 0.001 to 0.0055 for a moderate hardening material ($E/\sigma_0 = 500$, $n = 10$) capture the transition from a single void to a multiple void growth mechanism within the framework of plane-strain, SSY conditions with zero T-stress.
- Higher hardening materials ($E/\sigma_0 = 800$, $n = 5$) or the application of a negative T-stress suppress the multiple void growth mechanism, thereby increasing the crack growth resistance (J_R) curve.
- Computational cell analyses using the Gurson–Tvergaard constitutive model with calibrated q-parameters predict accurately the same J_R curves obtained using the discrete void approach.
- The new function, $h(\widehat{J})$, quantifies the increase in Weibull stress values caused by the additional volume of material sampled at high stress levels as the crack tip advances during ductile growth and by the stress concentrations that arise in material near the discrete voids.
- At equivalent external loading, $J/D\sigma_0$, increased values of initial porosity (f_0) increase the $h(\widehat{J})$ values and cumulative failure probability. This outcome stems from the coupled effect of greater stress concentrations due to the larger voids (and reduced ligament lengths) and to an increase in the material volume exposed to high stresses during small amounts of ductile tearing. Higher f_0 values lead to increased amounts of crack growth at a specified $J/D\sigma_0$, i.e., flat J_R curves.
- Small values of the Weibull modulus ($m = 8$) show little effect of the stress concentrations, with increased effects for larger values of $m = 12$ and 16.
- Higher hardening materials ($E/\sigma_0 = 800$, $n = 5$) suppress void growth and promote a single void growth mechanism and thus higher J_R curves. The reduced level of stress concentration at discrete voids lowers the relative Weibull stress values compared to the moderate hardening material at the same level of external loading.

- Plane-strain, SSY analyses including a negative T-stress applied proportionally with the external loading serve to approximate the response of low constraint fracture specimens. Such conditions promote a single void growth mechanism and higher J_R curves. Here we compute separately the constraint effects (g-function) due to the T-stress, and the coupled stress concentration and volume sampling effects (h-function) due to the discrete voids and ductile crack growth.
- The large element size employed in the computational cell analyses for ductile growth preclude sufficient resolution of the crack-front stress fields required for accurate computation of the Weibull stress. Comparisons here with the Weibull stress values obtained for discrete void models indicate clearly this problem. *Straightforward application of cell analyses to model growth with concurrent computation of the Weibull stress for cleavage models does not appear realistic*.

Future work in this area may include: examination of additional material flow properties and levels of applied T-stress, interaction between the initial root radius at the crack tip with the size and distance to the first void, the effects of constraint loss on the void growth process and the Weibull stress distribution using plane-strain fracture specimens, i.e., compact tension or single-edge notch bend specimens, more sophisticated methods for crack growth to improve the transition from void to void, models with voids arranged throughout the crack-front region and not limited to the crack plane, and eventually more complex 3D analysis.

Acknowledgment

This investigation was supported by grants principally from the U.S. Nuclear Regulatory Commission, Office of Regulatory Research and from the Naval Surface Warfare Center, Carderock Division. We wish to acknowledge the many valuable discussions with Dr. Kim Wallin, VTT (Finland) and Dr. Rob Tregoning, U.S. Nuclear Regulatory Commission (Washington, DC).

References

Anderson, T.L., 1995. Fracture Mechanics, Fundamentals and Applications. CRC Press, Boca Raton.

Aravas, N., McMeeking, R.M., 1985. Finite element analysis of void growth near a blunting crack tip. Journal of Mechanics and Physics of Solids 33, 25–49.

Bakker, A., Koers, R.W.J., 1991. Prediction of cleavage fracture events in the brittle–ductile transition region of a ferritic steel. In: Blauel, Schwalbe (Eds.), Defect Assessment in Components—Fundamentals and Applications, ESIS/EG9. Mechanical Engineering Publications, London, pp. 613–632.

Beremin, F.M., 1983. A local criterion for cleavage fracture of a nuclear pressure vessel steel. Metallurgical Transactions 14A, 2277–2287.

Bilby, B.A., Howard, I.C., Li, Z.H., 1994. Mesh independent cell models for continuum damage theory. Fatigue and Fracture of Engineering Materials and Structures 17, 1221–1233.

Broberg, K.B., 1994. Cell model of materials. Computational Mechanics 19, 447–452.

Curry, D.A., Knott, J.F., 1976. The relationship between fracture toughness and microstructure in the cleavage fracture of mild steel. Metal Science 10, 1–10.

Faleskog, J., Shih, C.F., 1997. Micromechanics of coalescence—I. Synergistic effects of elasticity, plastic yielding and multi-size-scale voids. Journal of Mechanics and Physics of Solids 45, 21–50.

Gao, X., Dodds, R.H., 2000. Constraint effects on the ductile-to-brittle transitions temperature of ferritic steels: a Weibull stress model. International Journal of Fracture 102, 43–69.

Gao, X., Faleskog, J., Shih, C.F., 1999. Analysis of ductile to cleavage transition in part-through cracks using a cell model incorporating statistics. Fatigue and Fracture of Engineering Materials and Structures 22, 239–250.

Gullerud, A., Dodds Jr., R.H., 2000. Simulation of ductile crack growth using computational cells: numerical aspects. Engineering Fracture Mechanics 66, 65–92.

Gurson, A.L., 1977. Continuum theory of ductile rupture by void nucleation and growth: part I—yield criteria and flow rules for porous ductile media. Journal of Engineering Materials and Technology 99, 2–15.

Howard, I.C., Li, Z.H., 2000. Finite element analysis of nonlocal effects in ductile fracture. Fatigue and Fracture of Engineering Materials and Structures 23, 817–824.

Isacsson, M., Nilsson, F., Faleskog, J., 1998. Probabilistic cell modeling of cleavage fracture. International Journal of Fracture 92, 359–372.

Koppenhoefer, K., Gullerud, A., Roy, A., Roychowdhury, S., Dodds Jr., R.H., 2001. WARP3D: dynamic non-linear analysis of solids using a preconditioned conjugate gradient software architecture. Structural Research Series (SRS) 596, UILU-ENG-94-2017, University of Illinois at Urbana-Champaign, 2001.

Kroon, M., 2001. Probabilistic Modeling of Cleavage Fracture. Licentiate Thesis, KTH, Department of Solid Mechanics, Royal Institute of Technology, Stockholm, Sweden.

Landes, J.D., Shaffer, D.H., 1980. Statistical characterization of fracture in the transition regionASTM STP 700. American Society for Testing and Materials, Philadelphia, pp. 368–382.

Larsson, S.G., Carlsson, A.J., 1973. Influence of non-singular stress terms and specimen geometry on small scale yielding at crack-tips in elastic–plastic materials. Journal of Mechanics and Physics of Solids 21, 447–473.

Lei, Y., O'Dowd, N.P., Busso, E.P., Webster, G.A., 1998. Weibull stress solutions for 2-D cracks in elastic and elastic–plastic materials. International Journal of Fracture 89, 245–268.

Lin, T., Evans, A.G., Ritchie, R.O., 1986. A statistical model of brittle fracture by transgranular cleavage. Journal of Mechanics and Physics of Solids 21, 263–277.

McMeeking, R.M., 1977. Finite deformation analysis of crack-tip opening in elastic–plastic materials and implications for fracture. Journal of Mechanics and Physics of Solids 25, 357–381.

Moran, B., Shih, C.F., 1987. A general treatment of crack tip contour integrals. International Journal of Fracture 35, 295–310.

Mudry, F., 1987. A local approach to cleavage fracture. Nuclear Engineering and Design 105, 65–76.

Neto, E.T., Ruggieri, C., 2001. Micromechanics characterization of constraint and ductile tearing effects in small scale yielding fracture. International Journal of Solids and Structures 38, 2171–2187.

Petti, J.P., Dodds Jr., R.H., 2004. Coupling of the Weibull stress model and macroscale models to predict cleavage fracture. Engineering Fracture Mechanics 71, 2079–2103.

Petti, J.P., Dodds Jr., R.H., 2005. Calibration of the Weibull scale parameter, σ_u, using the master curve. Engineering Fracture Mechanics 72, 91–120.

Rice, J.R., 1968. A path independent integral and the approximate analysis of strain concentration by notches and cracks. Journal of Applied Mechanics 35, 379–386.

Rice, J.R., Johnson, M.A., 1970. In: Kanninen, M.F. et al. (Eds.), Inelastic Behavior of Solids. McGraw-Hill, New York.

Ruggieri, C., Dodds, R.H., 1996a. A transferability model for brittle fracture including constraint and ductile tearing effects: a probabilistic approach. International Journal of Fracture 79, 309–340.

Ruggieri, C., Dodds Jr., R.H., 1996b. Probabilistic modeling of brittle fracture including 3-D effects on constraint loss and ductile tearing. Journal de Physique IV 6, C6-353–C6-362.

Ruggieri, C., Dodds Jr., R.H., 1998. Numerical evaluation of probabilistic fracture parameters with WSTRESS. Engineering Computations 15, 49–73.

Ruggieri, C., Panontin, T.L., Dodds Jr., R.H., 1996. Numerical modeling of ductile crack growth in 3-D using computational cell elements. International Journal of Fracture 82, 67–95.

Ruggieri, C., 2001. Influence of threshold parameters on cleavage fracture predictions using the Weibull stress model. International Journal of Fracture 110, 281–304.

Tvergaard, V., 1990. Material failure by void growth to coalescence. Advances in Applied Mechanics 27, 83–151.

Tvergaard, V., Hutchinson, J.W., 1992. The relation between crack growth resistance and fracture process parameters in elastic–plastic solids. Journal of Mechanics and Physics of Solids 40, 1377–1397.

Tvergaard, V., Hutchinson, J.W., 2002. Two mechanisms of ductile fracture: void by void growth versus multiple void interaction. International Journal of Solids and Structures 39, 3581–3597.

Tvergaard, V., Needleman, A., 1995. Effects of nonlocal damage in porous plastic solids. International Journal of Solids and Structures 32, 1063–1077.

Wallin, K., 1984. The scatter in K_{Ic}-results. Engineering Fracture Mechanics 19, 1085–1093.

Wallin, K., Saario, T., Torronen, K., 1984. Statistical model for carbide induced brittle fracture in steel. Metal Science 18, 13–16.

Xia, L., Cheng, L., 1997. Transition from ductile tearing to cleavage fracture: a cell-model approach. International Journal of Fracture 87, 289–306.

Xia, L., Shih, C.F., 1996. Ductile crack growth—III. Statistical aspects of cleavage fracture after tearing. Journal of Mechanics and Physics of Solids 44, 603–639.